

Research  
Green Chemical Engineering—Article

## Controlling the Reconstruction of Ni/CeO<sub>2</sub> Catalyst during Reduction for Enhanced CO Methanation



Xinyu Cao<sup>a</sup>, Tiancheng Pu<sup>a,b</sup>, Bar Mosevitzky Lis<sup>b</sup>, Israel E. Wachs<sup>b</sup>, Chong Peng<sup>c,\*</sup>, Minghui Zhu<sup>a,\*</sup>, Yongkang Hu<sup>d</sup>

<sup>a</sup> State Key Laboratory of Chemical Engineering, School of Chemical Engineering, East China University of Science and Technology, Shanghai 200237, China

<sup>b</sup> Operando Molecular Spectroscopy and Catalysis Research Laboratory, Department of Chemical and Biomolecular Engineering, Lehigh University, Bethlehem, PA 18015, USA

<sup>c</sup> Department of Instrument Science and Engineering, School of Electronic Information, Electrical Engineering, Shanghai Jiao Tong University, Shanghai 200240, China

<sup>d</sup> Dalian Research Institute of Petroleum and Petrochemicals, SINOPEC, Dalian 116045, China

### ARTICLE INFO

#### Article history:

Received 19 January 2021

Revised 30 April 2021

Accepted 17 August 2021

Available online 8 December 2021

#### Keywords:

Nickel–ceria catalyst

Catalyst activation

Crystallinity

Methanation

*In situ* spectroscopy

### ABSTRACT

Reductive pretreatment is an important step for activating supported metal catalysts but has received little attention. In this study, reconstruction of the supported nickel catalyst was found to be sensitive to pretreatment conditions. In contrast to the traditional activation procedure in hydrogen, activating the catalyst in syngas created supported Ni nanoparticles with a polycrystalline structure containing an abundance of grain boundaries. The unique post-activation catalyst structure offered enhanced CO adsorption and an improved CO methanation rate. The current strategy to tune the catalyst structure via manipulating the activation conditions can potentially guide the rational design of other supported metal catalysts.

© 2021 THE AUTHORS. Published by Elsevier LTD on behalf of Chinese Academy of Engineering and Higher Education Press Limited Company. This is an open access article under the CC BY-NC-ND license (<http://creativecommons.org/licenses/by-nc-nd/4.0/>).

### 1. Introduction

CO methanation is an important reaction to produce methane (CH<sub>4</sub>) from syngas, which can be obtained from the gasification of coal, biomass, and organic waste [1,2]. Nickel-based catalyst has been widely used for this reaction, with metallic Ni<sup>0</sup> as the active site. Thus, a reductive pretreatment (catalyst activation step) is required before the reaction to transform NiO<sub>x</sub> in the fresh catalyst to metallic Ni<sup>0</sup>. The number of exposed Ni<sup>0</sup> sites is one of the key indicators of catalytic activity. These sites are responsible for many critical elementary reaction steps such as C–O bond breaking, CH<sub>x</sub> hydrogenation, and CH<sub>4</sub> dissociation [3–5]. Therefore, creating more metallic Ni<sup>0</sup> sites is an efficient approach to the rational design of supported nickel catalysts.

Strategies that have been proposed to improve the performance of supported nickel catalysts focus on synthesis, for example, developing new preparation methods [6–12], modifying the nature of support [13–15], and doping with additional elements [16]. These strategies usually aim to create dispersed and thermally

stable Ni nanoparticles, generate more reactive facets, or enhance the kinetics of certain elementary steps. Furthermore, recent studies have revealed that the gas environment and temperature have an impact on the surface morphology of nickel-based catalysts. For example, introducing oxidizing gases (such as CO<sub>2</sub> and H<sub>2</sub>O) during the dry reforming of methane was found to result in encapsulation of Ni nanoparticles by a thin BO<sub>x</sub> layer evolved from the hexagonal boron nitride nanosheet support [17]. Exposing the supported Ni/SiO<sub>2</sub> catalyst to a CO<sub>2</sub>/H<sub>2</sub> or CH<sub>4</sub> environment at 800 °C created a surface Ni<sub>3</sub>C-like phase that exhibited an altered electronic structure and enhanced adsorption capacity of weakly bonded linear CO [18]. The effect of activation conditions on the catalyst performance, however, is usually overlooked. According to the literature, hydrogen is typically used as the reducing agent with the partial pressure, temperature, and duration common parameters to control the degree of reduction and particle size distribution [19,20].

Here, we investigated the effect of the reduction environment on the structure of supported Ni/CeO<sub>2</sub> catalyst. The crystal structure and surface morphology of metallic Ni nanoparticles were determined with *in situ* X-ray diffraction (XRD) and high-resolution transmission electron microscopy (HR-TEM). The chemical state of the catalyst was analyzed with *in situ* Raman, quasi *in situ* X-ray photoelectron spectroscopy (XPS) and quasi *in situ*

\* Corresponding authors.

E-mail addresses: [pengchong@dlut.edu.cn](mailto:pengchong@dlut.edu.cn) (C. Peng), [minghui Zhu@ecust.edu.cn](mailto:minghui Zhu@ecust.edu.cn) (M. Zhu).

high-sensitivity low-energy ion scattering (HS-LEIS). The surface species were probed with *in situ* diffuse reflectance infrared Fourier transform spectroscopy (DRIFTS). We report here for the first time that the surface structure of Ni/CeO<sub>2</sub> can be tuned by activating in CO methanation reactant (CO/H<sub>2</sub>) leading to improved catalytic performance toward the CO methanation reaction.

## 2. Materials and methods

### 2.1. Catalyst synthesis

The CeO<sub>2</sub> support was synthesized using a precipitation method with ammonium carbonate solution (30%; Aladdin Inc., China) as the precipitator. Briefly, cerium nitrate hexahydrate (99.95%, 0.928 g; Aladdin Inc.) was dissolved in 150 mL of deionized water. Under vigorous stirring, ammonium carbonate (4.8 g dissolved in 50 mL deionized water) solution was dropwise added. The resulting slurry was aged for 12 h and filtered. The solid was further dried at 60 °C for 12 h and eventually calcined at 500 °C for 4 h in air.

An incipient wetness impregnation method was employed to synthesize the supported Ni/CeO<sub>2</sub> catalyst. Briefly, nickel nitrate hexahydrate (Ni(NO<sub>3</sub>)<sub>2</sub>·6H<sub>2</sub>O, 98%, 0.779 g; Sinopharm Inc., China) was dissolved in 500 μL of deionized water. The solution was then slowly added into the as-prepared 1.8 g CeO<sub>2</sub> powders with continuous stirring for 1 h to form a slurry. The mixture was dried (60 °C, 12 h) and calcined (500 °C, 4 h) to obtain the catalyst. The nominal mass loading of NiO is 10 wt%. We determined the actual content of Ni to be 8.3 wt% with inductively coupled plasma optical emission spectroscopy (ICP-OES) analysis.

### 2.2. Catalyst activation

Two catalyst pretreatment conditions were employed to activate the supported Ni/CeO<sub>2</sub> catalyst. Unless otherwise described, these conditions are ① NiCe-H: 60%H<sub>2</sub>/40%N<sub>2</sub> (Air Liquide S.A., French), 50 standard cubic centimeters per minute (sccm), 450 °C, 2 h; and ② NiCe-CO: 60%H<sub>2</sub>/20%CO/20%N<sub>2</sub>, (Air Liquide S.A.), 50 sccm, 450 °C, 2 h.

### 2.3. Catalyst characterization

A transmission electron microscope (TEM, operated at a voltage of 200 kV; FEI Tecnai G2 F20 S-Twin, FEI Company, USA) was used to examine the morphologies of the catalysts. Energy dispersive X-ray spectroscopy (EDS) was used for elemental analysis.

The *in situ* Raman spectra were collected on a Horiba LabRam HR spectrometer (Horiba, Ltd., Japan) equipped with visible laser excitation with a wavelength of 514 nm (Light source: He–Cd), a 50× long working distance objective (Olympus BX-30-LWD, Olympus Corp., Japan), a single-stage monochromator, and a charge coupled device (CCD) detector (Horiba CCD-3000 V). The catalyst was activated for 2 h and exposed to CO methanation at 450 °C for 1 h with the spectra collected every 15 min.

The *in situ* XRD analysis was performed on a Bruker D8 ADVANCE X-ray powder diffractometer (Bruker Corp., USA) with a Cu K<sub>α</sub> ray source (λ = 0.154 nm) operating at 40 kV and 40 mA. The catalyst was treated in Ar at 450 °C and activated in different conditions. The XRD patterns were then collected from 20° to 80° with a resolution of 0.02°.

Quasi *in situ* XPS spectra were collected by Thermo ESCALAB 250Xi spectrometer (Thermo Fisher Scientific, USA) equipped with a monochromatic AlK radiation source (1486.6 eV (1 eV = 1.602176 × 10<sup>-19</sup> J), pass energy 20.0 eV). A pretreatment chamber was used for catalyst activation. The chamber was then evacuated,

and the sample was rapidly transferred into the analysis chamber in a vacuum without air contact.

The surface elemental distribution was analyzed with a Qtac 100 HS-LEIS spectrometer (ION-TOF, Germany) equipped with a double toroidal analyzer. The sample was prepared for analysis by compressing into Al<sub>2</sub>O<sub>3</sub> powder within a crucible at 2000 psi (1 psi = 6.894757 × 10<sup>3</sup> Pa). The pellet was loaded into the pretreatment chamber, dehydrated in the 10% O<sub>2</sub>/Ar environment at the temperature of 450 °C for 1 h, and activated under two conditions: ① 1:1 H<sub>2</sub>/Ar and ② 1:3 CO/H<sub>2</sub> at 350 °C for 2 h. Afterward, the pellet was transferred to the analysis chamber to avoid air contact. He<sup>+</sup> ions at 4 keV were used as the probe ion source, and Ar<sup>+</sup> ions with 0.5 keV were used for sputtering.

The H<sub>2</sub>-temperature programmed reduction (TPR) was conducted on an Autosorb-TP-5080-B (Xianquan Instrument Corp., China) connected to an online thermal conductivity detector (TCD). The temperature was ramped up to 800 °C at a rate of 10 °C·min<sup>-1</sup> with 10% H<sub>2</sub>/Ar at a flow rate of 30 sccm and held for 30 min.

The surface area of metallic Ni was estimated by measuring the amount of chemisorbed hydrogen molecules using a Micromeritics AutoChem II. The catalyst was pretreated at 450 °C in Ar and activated in different conditions. Afterward, the catalyst was purged with Ar to remove physically adsorbed H<sub>2</sub>, cooled to room temperature, and exposed to H<sub>2</sub> chemisorption pulses.

The *in situ* DRIFTS experiments were carried out on a PerkinElmer Frontier Fourier-transform infrared (FT-IR, PerkinElmer, Inc., USA) spectrometer equipped with a diffuse reflection cell (Harrick Praying Mantis, Harrick Scientific Products Inc., USA). About 50 mg of the catalyst was loaded into the reaction cell. The catalyst was first activated under different treatment conditions at 450 °C. Subsequently, the temperature was controlled at 300 °C, and the gas flow was switched to CO methanation for 1 h. The *in situ* DRIFTS spectra were collected every minute during the reaction.

### 2.4. Steady-state activity measurements

CO methanation performance was tested in a fixed-bed microreactor: 100 mg of catalyst powder was placed in a quartz tube, activated under different environments, and then evaluated for CO methanation reaction in 50 sccm of 20%CO/60%H<sub>2</sub>/20%N<sub>2</sub> and temperatures from 200 to 450 °C. All activity measurements were conducted at a gas hourly space velocity (GHSV) of 30 000 or 1 500 000 mL·g<sup>-1</sup>·h<sup>-1</sup>. The gas products were analyzed by online gas chromatography (Ruimin GC 2060, Ruimin Ltd., China). A 5A molecular sieve and a Porapak T column (Sigma-Aldrich Inc., USA) were used for gas separation. H<sub>2</sub> was detected by a TCD; hydrocarbons, CO<sub>2</sub>, and CO were detected by a flame ionization detector (FID) equipped with a methanizer.

## 3. Results and discussion

The supported Ni/CeO<sub>2</sub> catalyst was reduced at 450 °C for 2 h and evaluated for the CO methanation reaction. Two different environments were selected: 60%H<sub>2</sub>/40%N<sub>2</sub> and 20%CO/60%H<sub>2</sub>/20%N<sub>2</sub>; the reduced catalysts were denoted as NiCe-H and NiCe-CO, respectively. The NiCe-H catalyst exhibited a production rate of 146.3 mmol·g<sup>-1</sup>·h<sup>-1</sup> for CH<sub>4</sub> and 31.8 mmol·g<sup>-1</sup>·h<sup>-1</sup> for CO at 200 °C and 30 000 mL·g<sup>-1</sup>·h<sup>-1</sup> (Fig. 1(a), Table S1 in Appendix A). In comparison, NiCe-CO was more active toward CO methanation and catalyzed the formation of CH<sub>4</sub> at a rate of 163.0 mmol·g<sup>-1</sup>·h<sup>-1</sup>. The improvement in catalytic activity became more apparent at a higher GHSV of 1 500 000 mL·g<sup>-1</sup>·h<sup>-1</sup>. The production rate of CH<sub>4</sub> for NiCe-CO (121.8 mmol·g<sup>-1</sup>·h<sup>-1</sup>) increased by about 30% compared with NiCe-H (95.8 mmol·g<sup>-1</sup>·h<sup>-1</sup>).

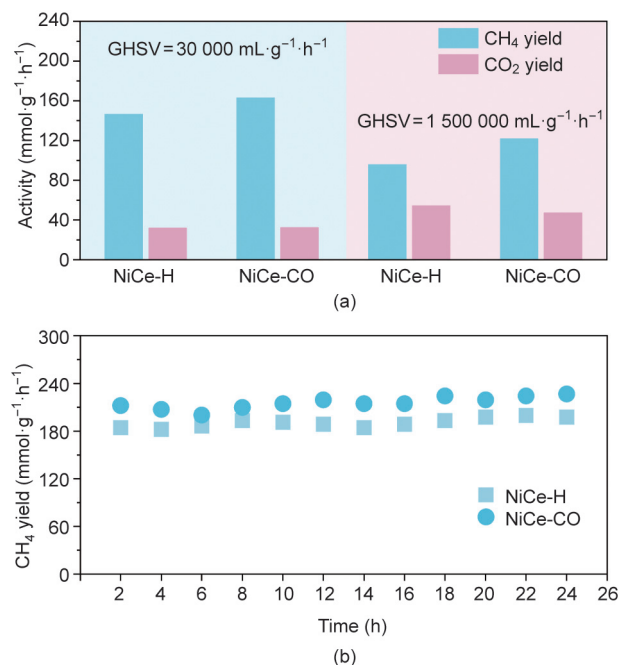


**Fig. 1.** (a) Activity toward production of CH<sub>4</sub> and CO over the supported Ni/CeO<sub>2</sub> activated under different conditions. (b) Long-term stability test result of Ni/CeO<sub>2</sub> activated under different conditions (reaction conditions:  $P = 1.0$  atm (1 atm =  $10^5$  Pa),  $T = 200$  °C, GHSV = 30 000 mL·g<sup>-1</sup>·h<sup>-1</sup>,  $n(\text{H}_2):n(\text{CO}) = 3:1$ ).

Reduction is necessary to activate the catalyst, and the unreduced catalyst has negligible activity toward the CO methanation reaction. Both activated catalysts exhibited very stable performances for 24 h (Fig. 1(b)), which implies that varying activation conditions may result in somewhat irreversible catalyst structural changes. We also evaluated the effect of activation condition on CO methanation over a Ni/CeO<sub>2</sub> catalyst with a higher nominal NiO loading of 50 wt%. The catalyst activated by reactants still showed better performance (Table S2 in Appendix A).

We analyzed the morphology of the supported Ni/CeO<sub>2</sub> catalyst after various activation pretreatments. The surface area and porosities appeared to be comparable (Figs. S1 and S2, and Table S3 in Appendix A) indicating that the aforementioned structural changes are most likely associated with the supported metallic Ni nanoparticles. HR-TEM images of the NiCe-H catalyst show large nanoparticles with lattice fringes of the Ni(111) facet (0.21 nm) (Fig. 2).

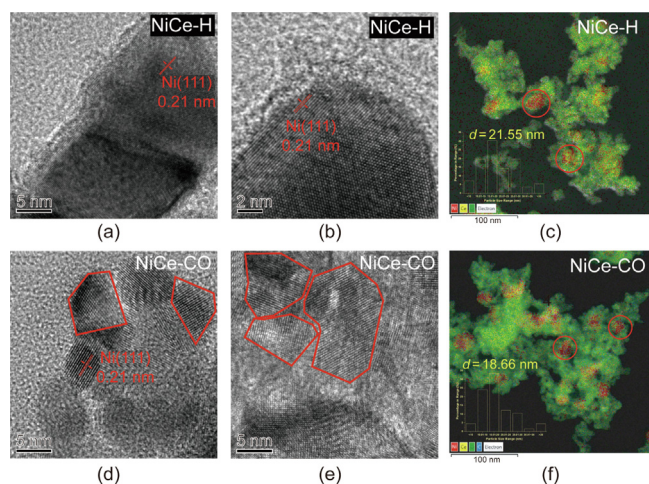


**Fig. 2.** HR-TEM images and elemental mappings for (a–c) NiCe-H and (d–f) NiCe-CO.

According to EDS mapping, the average size of metallic Ni nanoparticles was about 21.6 nm. Interestingly, while the apparent particle size of NiCe-CO obtained from EDS mapping (18.7 nm) was somewhat comparable to the hydrogen-treated catalysts, these Ni<sup>0</sup> particles presented in a polycrystalline state with nanosized grains (average diameter is 7.9 nm). The bulk structure of Ni/CeO<sub>2</sub> before and after activation was further probed with *in situ* XRD, which revealed a CeO<sub>2</sub> phase at 28.3°, 32.7°, 46.9°, and 55.8° (Fig. 3(a)). The crystallite size of CeO<sub>2</sub> was determined to be 11.8 nm using the Scherrer equation according to the CeO<sub>2</sub>(111) diffraction peak. It remained almost unchanged for NiCe-H (12.5 nm) and NiCe-CO (11.8 nm). The NiO phase could be detected for the fresh catalyst that featured a tiny NiO(200) peak at 43.1° corresponding to a crystallite size of 20.9 nm (Fig. S3 in Appendix A). NiCe-H had a diffraction peak at 44.0° that is characteristic of the Ni(111) phase. The crystallite size of Ni was 22.6 nm. However, the diffraction peak associated with metallic Ni could hardly be detected for NiCe-CO, which is consistent with the HR-TEM results.

The structure evolution of the catalyst during activation and reaction was also followed by time-resolved *in situ* Raman spectroscopy. The sharp peak at about 460 cm<sup>-1</sup> is assigned to the first-order F<sub>2g</sub> band, and the broad peak at about 590 cm<sup>-1</sup> is assigned to the defect-induced mode (D band) (Fig. 3(b)) [21–23]. The position of the F<sub>2g</sub> band is somewhat related to the number of defects (i.e., oxygen vacancies) in CeO<sub>2</sub>. The position can also be impacted by lattice strain and particle size [16,23,24]. Activation of Ni/CeO<sub>2</sub> creates oxygen vacancies as reflected by the intensified D band and red-shifted F<sub>2g</sub> band. These oxygen defects seem to be quite stable during the CO methanation reaction: The intensity of the D band remains almost unchanged.

Carbon deposition shows a D band at 1357 cm<sup>-1</sup> and a G band at 1585 cm<sup>-1</sup>. These form during activation via a mixture of CO and H<sub>2</sub> [25]. The formation of carbon species under CO-containing atmospheres has been previously well documented. For example, the activation of Pt/Co/Al<sub>2</sub>O<sub>3</sub> by 5%CO/He yielded a microporous carbon shell for Fischer–Tropsch synthesis [26]. Interestingly, exposing the hydrogen-activated catalyst to CO methanation reaction condition did not yield any carbon species regardless of the same gas environment and temperature as those applied to form NiCe-CO. Furthermore, the band intensities of the deposited carbon remained constant at the reaction stage. We speculate that the formation of carbon species only occurs along with the phase transformation of NiO to metallic Ni nanoparticles in a CO/H<sub>2</sub> environment. Such a feature may account for the excellent long-term stability (free of coke formation) during CO methanation as illustrated above.

The chemical state of the catalyst surface region was further investigated with quasi *in situ* XPS. Fresh Ni/CeO<sub>2</sub> exhibited Ni 2p spectra mainly contributed by Ni<sup>2+</sup> species at 855.0 eV (85%) with a minor amount of Ni<sup>0</sup> species at 853.2 eV (15%) (Fig. 4(a)). The Ni<sup>0</sup> species in the fresh catalyst is possibly due to the electronic interaction between oxygen-deficient CeO<sub>2-x</sub> species and NiO. After activation, the content of metallic Ni<sup>0</sup> species dramatically increased reaching 60% for NiCe-H and 66% for NiCe-CO. The XPS spectrum of the Ce 3d signal revealed the co-existence of Ce<sup>4+</sup> sites [Ce3d<sup>9</sup>4f<sup>0</sup>02p<sup>6</sup> ( $\mu'''$  and  $\nu'''$ ), Ce3d<sup>9</sup>4f<sup>1</sup>02p<sup>5</sup> ( $\mu''$  and  $\nu''$ ), and Ce3d<sup>9</sup>4f<sup>2</sup>02p<sup>4</sup> ( $\mu$  and  $\nu$ )] and Ce<sup>3+</sup> sites [Ce3d<sup>9</sup>4f<sup>2</sup>02p<sup>5</sup> ( $\mu_0$  and  $\nu_0$ ) and Ce3d<sup>9</sup>4f<sup>1</sup>02p<sup>6</sup> ( $\mu'$  and  $\nu'$ )] [27]. The percentage of Ce<sup>3+</sup> as a descriptor of oxygen vacancies was determined to be 16% for fresh Ni/CeO<sub>2</sub> (Fig. 4(b)). Consistent with the *in situ* Raman results, reduction pretreatment promoted the number of oxygen vacancies to 43% for NiCe-H and 46% for NiCe-CO, respectively. However, the corresponding O 1s spectra shows no difference for activated Ni/CeO<sub>2</sub> catalysts (Fig. S4 in Appendix A). Overall, our XPS results demonstrate that both of the two activation methods reduce the catalyst but with similar degrees of reduction and surface



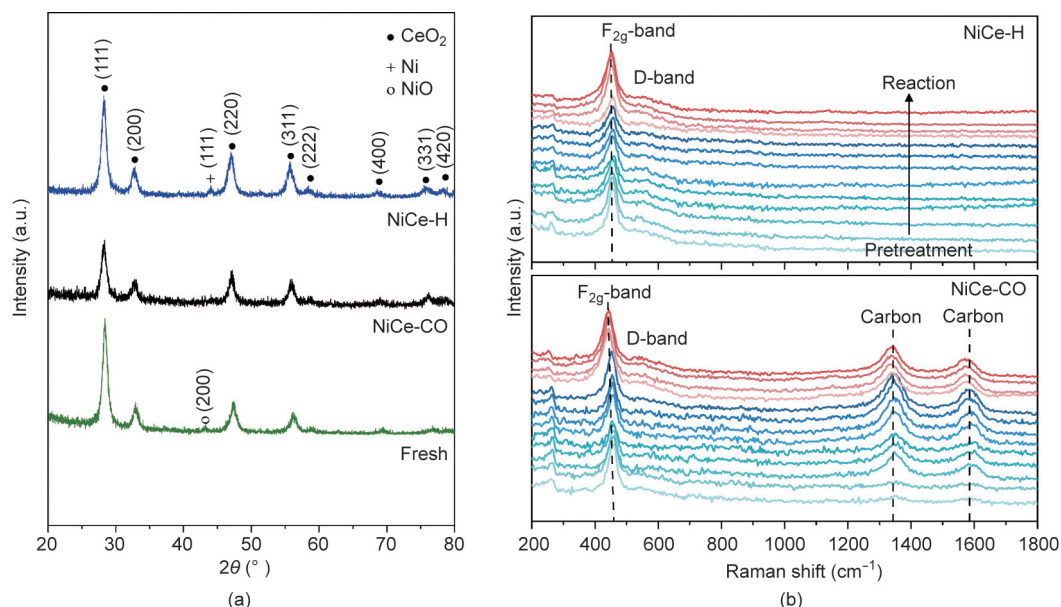


**Fig. 3.** (a) *In situ* XRD spectra of the supported Ni/CeO<sub>2</sub> catalysts. (b) Time-resolved *in situ* Raman spectra for NiCe-H and NiCe-CO during activation and reaction.

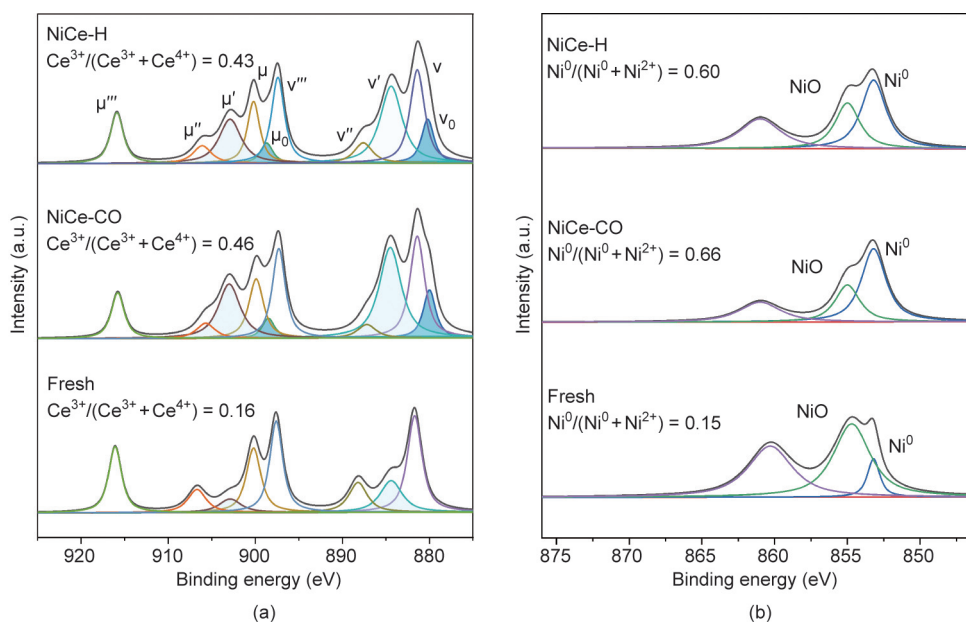


**Fig. 4.** Quasi *in situ* XPS spectra for Ni/CeO<sub>2</sub> activated in different environments show (a) the Ce 3d region and (b) the Ni 2p region.

elemental distribution (Table S4 in Appendix A). We also performed H<sub>2</sub>-TPR analysis on the Ni/CeO<sub>2</sub> catalysts, and the two activated catalysts revealed comparable H<sub>2</sub> uptake, which agrees nicely with the XPS findings (Fig. S5 in Appendix A).

The surface oxidation states of Ni and CeO<sub>2</sub> are not affected by adding CO during activation; thus, we hypothesize that the superior CO methanation performance of NiCe-CO is related to the polycrystalline nature of metallic nickel nanoparticles. Polycrystalline nanoparticles contain grain boundaries, which usually have superior catalytic activities [28–30]. Herein, the catalyst surface condition was probed with *in situ* DRIFTS analysis. The catalyst was activated, flushed with N<sub>2</sub>, and exposed to reactants at certain temperatures. Upon introducing CO methanation reactants at 300 °C, we observed surface formate species from the interaction of CO with surface hydroxyls and surface carbon-

ate species from the re-adsorption of CO<sub>2</sub> byproduct (Fig. S6 in Appendix A) [31]. Linearly adsorbed \*CO species progressively accumulates with slight redshift from about 2140 to 2050 cm<sup>-1</sup> (Figs. 5(a) and (b)) [31]. The \*CO species also form during activation by a mixture of CO/H<sub>2</sub> but without an apparent peak shift (Fig. 5(c)). The redshift of \*CO signal at the initial stage of the reaction is most likely associated with the reduction of mildly oxidized nickel surface that is generated during Ar flush. The infrared (IR) peak intensity of \*CO species for NiCe-CO appears to be much higher than that of NiCe-H (Fig. 5(d)), which suggests a larger number of CO adsorption sites (i.e., exposed Ni<sup>0</sup> sites) [32]. This could be further evidenced by the much greater uptake during H<sub>2</sub> chemisorption for NiCe-CO (1.24 m<sup>3</sup>·g<sup>-1</sup>) as compared with NiCe-H (0.85 m<sup>3</sup>·g<sup>-1</sup>) (Fig. S7 in Appendix A).

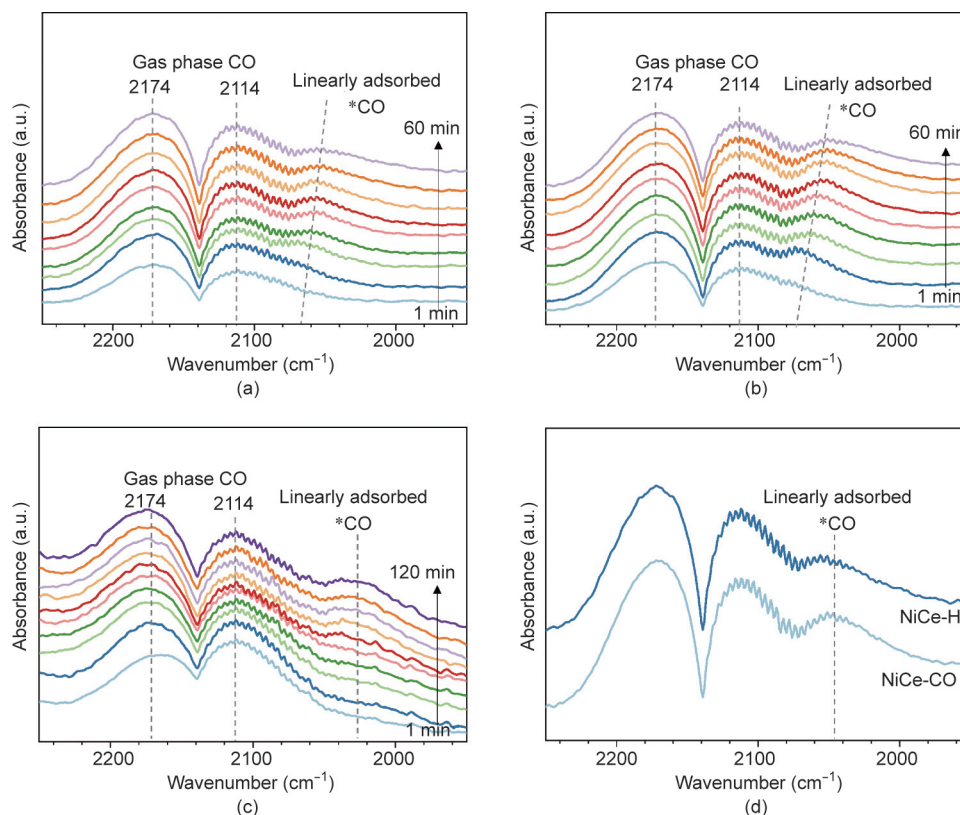


**Fig. 5.** *In situ* DRIFTS spectra of (a) NiCe-H and (b) NiCe-CO during the CO methanation reaction at 300 °C. (c) *In situ* DRIFTS spectra of Ni/CeO<sub>2</sub> during the activation in a CO/H<sub>2</sub> environment. (d) Comparison of IR spectra for NiCe-H and NiCe-CO after CO methanation at 300 °C for 60 min.

These data suggest a structure–activity relationship of activated Ni/CeO<sub>2</sub> catalysts. NiO is reduced to metallic Ni during the activation, which provides active site for C–O bond breaking and CH<sub>x</sub> hydrogenation [3,4]. Activating Ni/CeO<sub>2</sub> in a mixture of CO/H<sub>2</sub> results in carbon species being deposited onto the catalyst surface. Meanwhile, the Ni particles in NiCe-CO exhibit a polycrystalline morphology with nanosized grains. The current findings show a diverse distribution of Ni<sup>0</sup> facets after activation in CO/H<sub>2</sub>, which has yet to be reported. There are, however, many previous studies that describe the interaction between gas molecules/surface adsorbates and the catalyst surface during the reaction [33–36]. We hypothesize that our situation is due to the deposited carbon introducing anisotropic lattice strains at different locations of the nickel nanoparticles [37–39]. These carbon species might cover a portion of metallic Ni nanoparticles. However, the catalyst still contained abundant exposed Ni<sup>0</sup> sites because the quasi *in situ* HS-LEIS analysis shows Ni atoms on the outermost surface layer of both NiCe-H and NiCe-CO (Fig. S8 in Appendix A). Unless polymeric carbon or dense ordered graphite layers are formed, these carbon species are usually porous and have a minor effect on the catalytic activity [40]. The polycrystalline nature of reactant-activated catalyst results in many grain boundaries showing greater CO adsorption capacity and higher apparent methanation activity. The intrinsic reaction kinetics of CO methanation reactions at the nickel grain boundary sites, however, have yet to be elucidated and require further detailed kinetic and theoretical analyses.

#### 4. Conclusions

To summarize, different pretreatment conditions were found to affect the surface structure of the supported Ni/CeO<sub>2</sub> catalyst. In contrast to the traditional activation procedure in hydrogen, acti-

vating the catalyst in a mixture of CO/H<sub>2</sub> creates polycrystalline Ni nanoparticles that possess abundant grain boundaries with a larger CO adsorption capacity, which benefits CO methanation. The formation of polycrystalline Ni nanoparticles may be related to carbon deposition on the surface. This work provides a new strategy to optimize the catalyst structure by manipulating activation conditions.

#### Acknowledgments

This work is sponsored by the National Natural Science Foundation of China (22078089 and 22122807), Natural Science Foundation of Shanghai (21ZR1425700), Program for Professor of Special Appointment (Eastern Scholar) at Shanghai Institutions of Higher Learning and Shanghai Sailing Program (19YF1410600). The research at Lehigh University was supported by the Center for Understanding and Control of Acid Gas-Induced Evolution of Materials for Energy (UNCAGE-ME), an Energy Frontier Research Center funded by Department of Energy, Office of Science, Office of Basic Energy Sciences (DE-SC0012577).

#### Compliance with ethics guidelines

Xinyu Cao, Tiancheng Pu, Bar Mosevitzky Lis, Israel E. Wachs, Chong Peng, Minghui Zhu, and Yongkang Hu declare that they have no conflict of interest or financial conflicts to disclose.

#### Appendix A. Supplementary data

Supplementary data to this article can be found online at <https://doi.org/10.1016/j.eng.2021.08.023>.

## References

- [1] Liu J, Cui D, Yao C, Yu J, Su F, Xu G. Syngas methanation in fluidized bed for an advanced two-stage process of SNG production. *Fuel Process Technol* 2016;141:130–7.
- [2] Rönisch S, Schneider J, Matthischke S, Schlüter M, Götz M, Lefebvre J, et al. Review on methanation—from fundamentals to current projects. *Fuel* 2016;166:276–96.
- [3] Blligaard T, Nørskov JK, Dahl S, Matthiesen J, Christensen CH, Sehested J. The Brønsted–Evans–Polanyi relation and the volcano curve in heterogeneous catalysis. *J Catal* 2004;224(1):206–17.
- [4] van Meerten RZC, Vollenbroek JG, de Croon MHJM, van Nisselrooy PFMT, Coenen JWE. The kinetics and mechanism of the methanation of carbon monoxide on a nickel–silica catalyst. *Appl Catal* 1982;3(1):29–56.
- [5] Tsiouriari VA, Veyrkios XE. Carbon and oxygen reaction pathways of CO<sub>2</sub> reforming of methane over Ni/La<sub>2</sub>O<sub>3</sub> and Ni/Al<sub>2</sub>O<sub>3</sub> catalysts studied by isotopic tracing techniques. *J Catal* 1999;187(1):85–94.
- [6] Tian H, Li Z, Feng G, Yang Z, Fox D, Wang M, et al. Stable, high-performance, dendrite-free, seawater-based aqueous batteries. *Nat Commun* 2021;12(1):237.
- [7] Pan F, Yang Y. Designing CO<sub>2</sub> reduction electrode materials by morphology and interface engineering. *Energy Environ Sci* 2020;13(8):2275–309.
- [8] Chee SW, Arce-Ramos JM, Li W, Genest A, Mirsaidov U. Structural changes in noble metal nanoparticles during CO oxidation and their impact on catalyst activity. *Nat Commun* 2020;11:2133.
- [9] Beniya A, Higashi S, Ohba N, Jinnouchi R, Hirata H, Watanabe Y. CO oxidation activity of non-reducible oxide-supported mass-selected few-atom Pt single-clusters. *Nat Commun* 2020;11:1888.
- [10] Liu Q, Yang H, Dong H, Zhang W, Bian B, He Q, et al. Effects of preparation method and Sm<sub>2</sub>O<sub>3</sub> promoter on CO methanation by a mesoporous NiO–Sm<sub>2</sub>O<sub>3</sub>/Al<sub>2</sub>O<sub>3</sub> catalyst. *New J Chem* 2018;42(15):13096–106.
- [11] Liu Q, Tian Y. One-pot synthesis of NiO/SBA-15 monolith catalyst with a three-dimensional framework for CO<sub>2</sub> methanation. *Int J Hydrogen Energy* 2017;42(17):12295–300.
- [12] Zhang J, Xin Z, Meng X, Tao M. Synthesis, characterization and properties of anti-sintering nickel incorporated MCM-41 methanation catalysts. *Fuel* 2013;109:693–701.
- [13] Kamata H, Tian ZQ, Izumi Y, Choong CKS, Chang J, Schreyer M, et al. Dispersed and high loading Ni catalyst stabilized in porous SiO<sub>2</sub> matrix for substituted natural gas production. *Catal Today* 2018;299:193–200.
- [14] Ebadi A, Tourani S, Khorasheh F. Synthesis of highly dispersed nanosized NiO/MgO–Al<sub>2</sub>O<sub>3</sub> catalyst for the production of synthetic natural gas with enhanced activity and resistance to coke formation. *Ind Eng Chem Res* 2018;57(38):12700–14.
- [15] Lin X, Lin L, Huang K, Chen X, Dai W, Fu X. CO methanation promoted by UV irradiation over Ni/TiO<sub>2</sub>. *Appl Catal B Environ* 2015;168–169:416–22.
- [16] Zhu M, Tian P, Cao X, Chen J, Pu T, Shi B, et al. Vacancy engineering of the nickel-based catalysts for enhanced CO<sub>2</sub> methanation. *Appl Catal B Environ* 2021;282:119561.
- [17] Dong J, Fu Q, Li H, Xiao J, Yang B, Zhang B, et al. Reaction-induced strong metal–support interactions between metals and inert boron nitride nanosheets. *J Am Chem Soc* 2020;142:17167–74.
- [18] Galhardo TS, Braga AH, Arpini BH, Szanyi J, Gonçalves RV, Zornio BF, et al. Optimizing active sites for high CO selectivity during CO<sub>2</sub> hydrogenation over supported nickel catalysts. *J Am Chem Soc* 2021;143(11):4268–80.
- [19] Kokka A, Ramantani T, Petala A, Panagiotopoulou P. Effect of the nature of the support, operating and pretreatment conditions on the catalytic performance of supported Ni catalysts for the selective methanation of CO. *Catal Today* 2020;355:832–43.
- [20] Du G, Lim S, Yang Y, Wang C, Pfefferle L, Haller G. Methanation of carbon dioxide on Ni-incorporated MCM-41 catalysts: the influence of catalyst pretreatment and study of steady-state reaction. *J Catal* 2007;249(2):370–9.
- [21] Yang C, Yang J, Duan X, Hu G, Liu Q, Ren S, et al. Roles of photo-generated holes and oxygen vacancies in enhancing photocatalytic performance over CeO<sub>2</sub> prepared by molten salt method. *Adv Powder Technol* 2020;31(9):4072–81.
- [22] Kosacki I, Petrovsky V, Anderson HU, Colomban P. Raman spectroscopy of nanocrystalline ceria and zirconia thin films. *J Am Ceram Soc* 2002;85:2646–50.
- [23] Wu Z, Li M, Howe J, Meyer HM, Overbury SH. Probing defect sites on CeO<sub>2</sub> nanocrystals with well-defined surface planes by Raman spectroscopy and O<sub>2</sub> adsorption. *Langmuir* 2010;26(21):16595–606.
- [24] Spanier JE, Robinson RD, Zhang F, Chan SW, Herman IP. Size-dependent properties of CeO<sub>2</sub> nanoparticles as studied by Raman scattering. *Phys Rev B* 2001;64:245407.
- [25] Dresselhaus MS, Jorio A, Hofmann M, Dresselhaus G, Saito R. Perspectives on carbon nanotubes and graphene Raman spectroscopy. *Nano Lett* 2010;10:751–8.
- [26] Jalama K, Ma W, Jacobs G, Sparks D, Qian D, Davis BH. Fischer–Tropsch synthesis over Pt/Co/Al<sub>2</sub>O<sub>3</sub> catalyst: improvement in catalyst stability by activation with diluted CO. *Appl Catal A Gen* 2020;602:117645.
- [27] Bèche E, Charvin P, Perarnau D, Abanades S, Flamant G. Ce 3d XPS investigation of cerium oxides and mixed cerium oxide (Ce<sub>x</sub>Ti<sub>y</sub>O<sub>2</sub>). *Surf Interface Anal* 2008;40(3–4):264–7.
- [28] Mariano RG, McKelvey K, White HS, Kanan MW. Selective increase in CO<sub>2</sub> electroreduction activity at grain-boundary surface terminations. *Science* 2017;358(6367):1187–92.
- [29] Feng X, Jiang K, Fan S, Kanan MW. Grain-boundary-dependent CO<sub>2</sub> electroreduction activity. *J Am Chem Soc* 2015;137(14):4606–9.
- [30] Chen Z, Wang T, Liu B, Cheng D, Hu C, Zhang G, et al. Grain-boundary-rich copper for efficient solar-driven electrochemical CO<sub>2</sub> reduction to ethylene and ethanol. *J Am Chem Soc* 2020;142(15):6878–83.
- [31] Jia X, Zhang X, Rui N, Hu X, Liu C. Structural effect of Ni/ZrO<sub>2</sub> catalyst on CO<sub>2</sub> methanation with enhanced activity. *Appl Catal B Environ* 2019;244:159–69.
- [32] Tang H, Su Y, Zhang B, Lee AF, Isaacs MA, Wilson K, et al. Classical strong metal–support interactions between gold nanoparticles and titanium dioxide. *Sci Adv* 2017;3:1–9.
- [33] Tao F, Grass ME, Zhang Y, Butcher DR, Renzas JR, Liu Z, et al. Reaction-driven restructuring of Rh–Pd and Pt–Pd core–shell nanoparticles. *Science* 2008;322(5903):932–4.
- [34] Lee AF, Ellis CV, Naughton JN, Newton MA, Parlett CMA, Wilson K. Reaction-driven surface restructuring and selectivity control in allylic alcohol catalytic aerobic oxidation over Pd. *J Am Chem Soc* 2011;133(15):5724–7.
- [35] Chen S, Abdel-Mageed AM, Dyballa M, Parlinska-Wojtan M, Bansmann J, Pollastri S, et al. Raising the CO<sub>x</sub> methanation activity of a Ru/γ-Al<sub>2</sub>O<sub>3</sub> catalyst by activated modification of metal–support interactions. *Angew Chem Int Ed* 2020;59(50):22763–70.
- [36] van Deelen TW, Hernández Mejía C, de Jong KP. Control of metal–support interactions in heterogeneous catalysts to enhance activity and selectivity. *Nat Catal* 2019;2(11):955–70.
- [37] Chaudhri MM. Subsurface strain distribution around Vickers hardness indentations in annealed polycrystalline copper. *Acta Mater* 1998;46(9):3047–56.
- [38] Ghosh R, Basak D, Fujihara S. Effect of substrate-induced strain on the structural, electrical, and optical properties of polycrystalline ZnO thin films. *J Appl Phys* 2004;96(5):2689–92.
- [39] Adelung R, Aktas OC, Franc J, Biswas A, Kunz R, Elbahri M, et al. Strain-controlled growth of nanowires within thin-film cracks. *Nat Mater* 2004;3(6):375–9.
- [40] Zhang Y, Cao C, Zhang C, Zhang Z, Liu X, Yang Z, et al. The study of structure-performance relationship of iron catalyst during a full life cycle for CO<sub>2</sub> hydrogenation. *J Catal* 2019;378:51–62.